Frustrated magnetic cycloidal structure and emergent Potts nematicity in $CaMn_2P_2$

Farhan Islam,[1,2] Thaís V. Trevisan,[1,2] Thomas Heitmann,[3] Santanu Pakhira,[1] Simon X. M. Riberolles,[1] N. S. Sangeetha,[1,*] David C. Johnston,[1,2] Peter P. Orth,[1,2] and David Vaknin[1,2,†]

[1]*Ames National Laboratory, Iowa State University, Ames, Iowa 50011, USA*

[2]*Department of Physics and Astronomy, Iowa State University, Ames, Iowa 50011, USA*

[3]*The Missouri Research Reactor and Department of Physics and Astronomy, University of Missouri, Columbia, Missouri 65211, USA*

(Received 4 October 2022; accepted 7 February 2023; published 21 February 2023)

We report neutron-diffraction results on single-crystal $CaMn_2P_2$ containing corrugated Mn honeycomb layers, and we determine its ground-state magnetic structure. The diffraction patterns consist of prominent (1/6,1/6,L) reciprocal-lattice unit (r.l.u.; L = integer) magnetic Bragg reflections, whose temperature-dependent intensities are consistent with a first-order antiferromagnetic phase transition at the Néel temperature $T_N = 70(1)$ K. Our analysis of the diffraction patterns reveals an in-plane 6×6 magnetic unit cell with ordered spins that in the principal-axis directions rotate by 60° steps between nearest neighbors on each sublattice that forms the honeycomb structure, consistent with the P_Ac magnetic space group. We find that a few other magnetic subgroup symmetries (P_A2/c, P_C2/m, $P_S\bar{1}$, P_C2, P_Cm, P_S1) of the paramagnetic $P\bar{3}m11'$ crystal symmetry are consistent with the observed diffraction pattern. We relate our findings to frustrated J_1-J_2-J_3 Heisenberg honeycomb antiferromagnets with single-ion anisotropy and the emergence of Potts nematicity.

DOI: 10.1103/PhysRevB.107.054425

I. INTRODUCTION

Magnetic materials with local moments arranged on a honeycomb lattice are known to exhibit a variety of complex magnetic states in the presence of frustrated spin exchange interactions. Recent examples are the honeycomb iridates [1,2], the nickelate $Ni_2Mo_3O_8$ [3], transition-metal oxides $InCu_{2/3}V_{1/3}O_3$ [4,5], $Bi_3Mn_4O_{12}(NO_3)$ [6], and verdazyl-based salts [7]. Often the complex behavior of these systems can be rationalized using quantum spin models such as the Kitaev-Heisenberg honeycomb model [8–11] or the J_1-J_2-J_3 Heisenberg honeycomb model [12–23]. The former exhibits various complex magnetically ordered phases and a quantum-spin-liquid ground state when Kitaev interactions are dominant and the local moments a low spin, $S = 1/2, 1, 3/2$ [8,24,25]. The latter hosts different collinear and noncollinear magnetic states, including complex spirals, already in the classical limit, and its phase diagram also includes magnetically disordered regions with intriguing valence-bond correlations for $S = 1/2$ [16]. Specifically, for $J_3 = 0$, the classical J_1-J_2 Heisenberg honeycomb antiferromagnet exhibits a Néel-ordered ground state for $J_2 < J_1/6$ and degenerate single-Q spiral states for $J_2 > J_1/6$ [12–15]. Nonzero J_3 or, alternatively, quantum and thermal fluctuations [15] lift this continuous degeneracy and select six symmetry-related wavevectors out of the degenerate manifold.

Another rich experimental platform for frustrated honeycomb magnets consists of the trigonal compounds $CaMn_2P_2$, $CaMn_2As_2$, $CaMn_2Sb_2$, $CaMn_2Bi_2$, $SrMn_2P_2$, $SrMn_2As_2$, and $SrMn_2As_2$ with space group $P\bar{3}m1$ (no. 164) [26–32] and associated point group D_{3d}. As shown in Fig. 1, these systems contain the transition-metal element Mn in a corrugated honeycomb structure, which is formed by two adjacent trigonal layers (or sublattices) that are stacked in an A-B type fashion. The Mn atoms occupy Wyckoff positions 2d with site symmetry 3m. There are two Mn atoms per unit cell, which form the A,B sublattice sites of the honeycomb lattice. The transition-metal bilayer magnetic moments have no intervening binding atoms, as shown in Fig. 1(a), so that the major magnetic coupling between nearest neighbors is likely a direct Mn-Mn coupling, and couplings among next-nearest neighbors (NNNs) are likely due to Mn-Pn-Mn superexchange. Neutron diffraction measurements of Mn compounds with Pn = As, Sb, or Bi have revealed a simple Néel-type magnetic structure in $SrMn_2As_2$, $CaMn_2Sb_2$, and $CaMn_2Bi_2$ [28,30,32,33]. This Néel magnetic structure is shown schematically in Fig. 1(b). For $CaMn_2Sb_2$, it has been suggested that the moments are slightly canted towards the c-axis [31]. These observations are consistent with a dominant NN interaction $J_1 \gg J_2$ for these materials.

It has recently been concluded that the superexchange within an Mn-Pn-Mn moiety increases as the atomic number of Pn is reduced, thereby increasing the magnetic frustration in the system. Thus, NNN interactions are expected to be stronger for Pn = P than for Pn = Bi for similar bond configurations [34]. We thus expect $CaMn_2P_2$ to experience a sizable NNN coupling J_2 and thus substantial magnetic frustration, which is one of the main motivations for this work.

Here, we report neutron-diffraction results on single crystals of $CaMn_2P_2$, and we determine its ground-state magnetic structure. Recent ^{31}P NMR measurements [26] indicate that

*Present address: Institute for Experimental Physics IV, Ruhr University Bochum, 44801 Bochum, Germany.

†vaknin@ameslab.gov

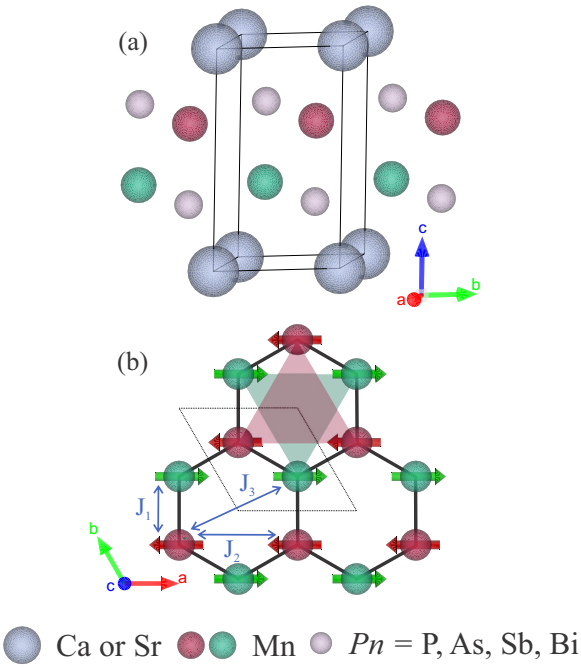

FIG. 1. (a) Chemical structure of AMn_2Pn_2 (A = Sr, Ca; Pn = P, As, Sb, Bi) showing the Mn trigonal bilayer without intervening elements. (b) Projection of the two trigonal Mn sublattices onto the *ab*-plane, shown with red and green shades. The A and B layers are stacked with two atoms per unit cell (the dotted rhombus shows the basal unit cell). The Mn bilayer forms a corrugated honeycomb lattice, where the nearest-neighbor (NN) interactions (J_1), the next-nearest-neighbor (NNN) interactions (J_2), and the third-neighbor interactions (J_3) are indicated. The magnetic structure shown is typical for the AMn_2Pn_2 compounds with Pn = As, Sb, Bi, for which the first-neighbor interactions are dominant and antiferromagnetic: $J_1 \gg J_2, J_3$. In contrast, here we report that $CaMn_2P_2$ exhibits a different magnetic structure that emerges mainly due to frustrated couplings $J_1/2 \approx J_2$. (Although implied in the figure, $SrMn_2Bi_2$ has not yet been synthesized or discussed in the literature.)

the magnetic structure of $CaMn_2P_2$ is commensurate with the lattice. This is in contrast to $SrMn_2P_2$, which is found to possess an incommensurate magnetic order [26]. These observations are consistent with neutron-diffraction measurements of $SrMn_2P_2$ that indicate a complex and as yet undetermined magnetic structure [35]. Interestingly, $CaMn_2P_2$ and $SrMn_2P_2$ have recently been reported to undergo an unusual first-order antiferromagnetic (AFM) transition at $T_N = 70(3)$ and 53(1) K, respectively [26]. By contrast, the isostructural $CaMn_2As_2$ and $SrMn_2As_2$ compounds undergo second-order AFM transitions [27]. Below, we relate the observed first-order magnetic transition in $CaMn_2P_2$ with its more complex spiral magnetic order that breaks threefold rotational symmetry and promotes the emergence of a Potts-nematic order parameter [15,36,37].

We note that AMn_2Pn_2 (A = Ca or Sr and Pn = P, As, Sb) compounds display strong two-dimensional (2D) magnetic fluctuations as manifested in magnetic susceptibility (χ) measurements that do not show Curie-Weiss behavior at temperatures much higher than T_N [26,30–33]. In addition, the $\chi(T)$ with applied magnetic field along the *ab*-plane for all these compounds hardly shows any anomaly at T_N. This 2D behavior also manifests in the magnetic order parameter in neutron-diffraction measurements of $SrMn_2As_2$ [30]. These characteristics indicate that the dominant in-plane NN coupling J_1 is AFM and is likely much larger than the interlayer couplings between honeycomb planes, leading to sizable 2D AFM correlations above T_N. Interestingly, inelastic neutron-scattering measurements that were analyzed using spin-wave theory for the J_1-J_2 Heisenberg model determined a ratio of $J_2/J_1 \approx 1/6$ for $CaMn_2Sb_2$. This places the system in proximity to a tricritical point that separates a Néel-ordered phase and two different spiral magnetic phases [14,18,38].

II. EXPERIMENTAL DETAILS AND METHODS

Single crystals of $CaMn_2P_2$ were grown in Sn flux, as described previously [26], and the crystal used in this study is from the same growth batch. Single-crystal neutron-diffraction experiments were performed in zero applied magnetic field using the TRIAX triple-axis spectrometer at the University of Missouri Research Reactor (MURR). An incident neutron beam of energy 14.7 meV was directed at the sample using a pyrolytic-graphite (PG) monochromator. A PG analyzer was used to reduce the background. Shorter neutron wavelengths were removed from the primary beam using PG filters placed before the monochromator and in between the sample and analyzer. Beam divergence was limited using collimators before the monochromator; between the monochromator and sample; sample and analyzer; and analyzer and detector of $60' - 60' - 40' - 40'$, respectively. A 40 mg $CaMn_2P_2$ crystal was mounted on the cold tip of an Advanced Research Systems closed-cycle refrigerator with a base temperature of approximately 5 K. The crystal was mounted in the $(H, 0, L)$ and (H, H, L) scattering planes. We measured the lattice parameters to be $a = 4.096(1)$ and $c = 6.848(2)$ Å at base temperature. We also note that our sample consists of at least two twins that are disoriented with respect to each other, as indicated in Fig. 2. Our diffraction patterns here and below also show Bragg reflections from the polycrystalline Al sample holder.

III. EXPERIMENTAL RESULTS AND ANALYSIS

A. Experimental results

Diffraction scans along the $(H, H, 1)$ direction at $T = 6$ and 100 K in Fig. 2(a) show the emergence of a prominent peak at $H = 1/6$ r.l.u. (reciprocal-lattice units) at low temperatures. As shown in Fig. 2(b), the difference between these scans at 6 and 100 K displays magnetic Bragg peaks at $(\eta, \eta, 1)$ and $(1 - \eta, 1 - \eta, 1)$, where $\eta = 1/6$. Figure 3(a) shows the difference between scans at 6 and 100 K along $(-\eta, -\eta, L)$, indicating magnetic Bragg peaks at $L = -3, -2, -1, 1, 2$, and 3. Figure 3(b) shows similar observations of magnetic Bragg peaks at $L = 1$, 2, and 3 in the direction of (η, η, L). Scans along $(H, H, 0)$ do not show any newly emerging peaks at low temperatures (not shown). Figure 3(c) shows the difference of scans along $(H, 0, 0)$ at 6 and 100 K with a weak peak at the nuclear (1,0,0) reflection and possibly another very weak one at (2,0,0). The other signals that have a negative intensity originate from the Al sample

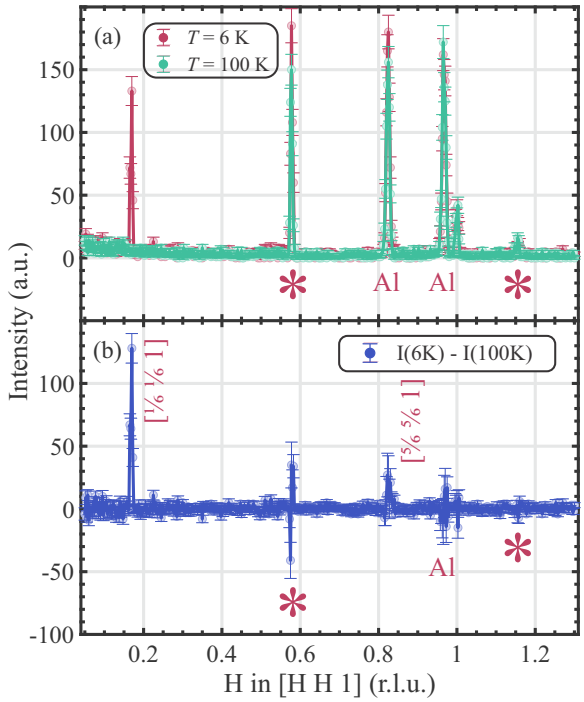

FIG. 2. (a) Diffraction patterns along $(H, H, 1)$ at $T = 6$ and 100 K showing the emergence of a prominent peak at $H = 1/6$ r.l.u. (b) The difference between the $(H, H, 1)$ patterns at 6 and 100 K showing that the observed magnetic Bragg reflections in this direction are $(\eta, \eta, 1)$ and $(1 - \eta, 1 - \eta, 1)$, where $\eta = 1/6$. Al peaks (originating from the sample holder) in the difference pattern show both positive and negative signals due to the thermal shift in peak positions. The peaks with asterisks originate from a twin of $CaMn_2P_2$ oriented in a different direction.

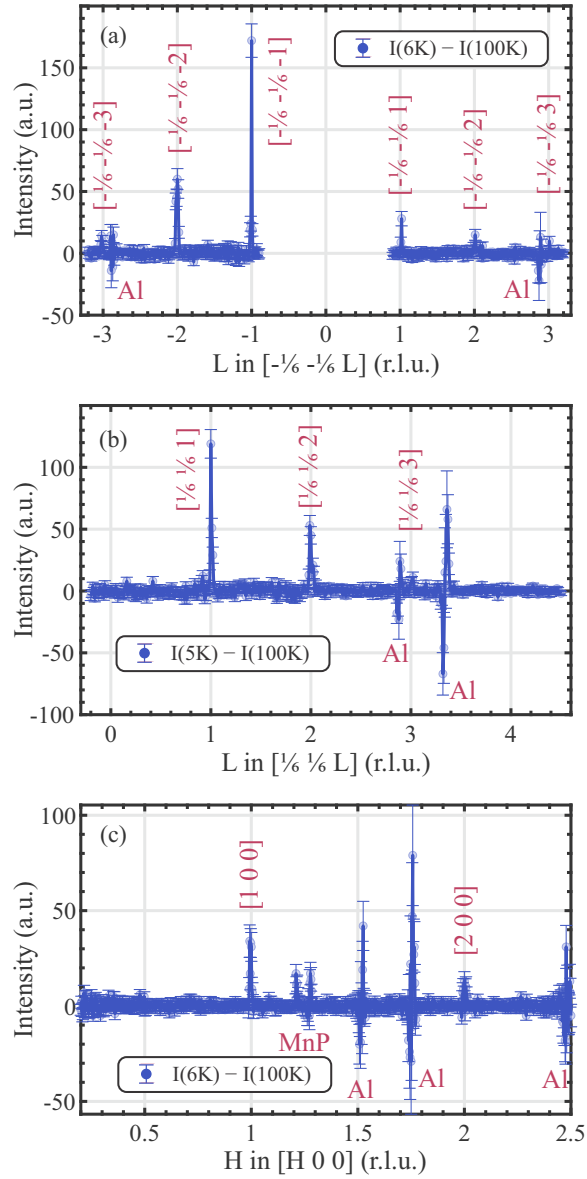

FIG. 3. Difference between scans at low and high temperature, as indicated, along (a) $(-1/6, -1/6, L)$ showing peaks at integer values of L between -3 and 3 (except for $L = 0$); (b) $(1/6, 1/6, L)$ showing peaks at the integer values of L between 1 and 3 (scans with negative L were not accessible due to the experimental setup); and (c) $(H, 0, 0)$ showing a weak peak at the nuclear (1,0,0) position and possibly another at (2,0,0). Signals from the Al sample holder are marked in the figures. As indicated in (c), a minute inclusion of ferromagnetic MnP crystals gives rise to weak peaks.

holder. Also, magnetic peaks from a small amount of MnP in the crystal are present in the scan, as indicated. The temperature dependence of (1,0,0) does not exhibit a transition at T_N. This implies that the splitting is not significantly related to the observed magnetic structure.

The temperature dependence of the integrated intensity of the $(\eta, \eta, 1)$ reflections in Fig. 4 shows a very sharp transition at $T = 70(1)$ K that coincides with a previous report indicating a strong first-order magnetic phase transition at this temperature [26]. The fact that the peak intensities of the $(\pm\eta, \pm\eta, L)$ reflections fall off for larger L, as expected from the magnetic form factor of Mn^{2+}, is further evidence that these newly observed Bragg peaks are magnetic in origin. Below, we propose various related magnetic structures that are consistent with the experimental observations assuming the magnetic propagation vector is $\boldsymbol{\tau} = (\eta, \eta, 0)$ r.l.u. with $\eta = 1/6$.

B. Analysis of experimental results

The observed $(\eta, \eta, 0)$ propagation vector indicates that the magnetic structure consists of a 6×6 nuclear basal unit cell. Figure 5(a) is a compilation of the magnetic reflections observed in the (H, H, L) plane, where the sizes of the circles (i.e., peaks) approximate the observed intensities. A systematic analysis reveals that there are seven magnetic space groups (MSGs) that are consistent with the observed magnetic-diffraction patterns. These are P_A2/c, P_C2/m, P_Ac, $P_S\bar{1}$, P_C2, P_Cm, and P_S1 (see Fig. 6). The first two have higher symmetry, and P_Ac, P_C2 are descendants of P_A2/c, while $P_S\bar{1}$, P_C2, and P_Cm are descendants of P_C2/m, and the group P_S1 has the lowest symmetry (see Fig. 3 and Appendix B for details).

We now describe an intuitive approach to the magnetic model structure (corresponding to P_Ac), which is constructed by creating a 6×6 in-plane nuclear unit cell that spans the

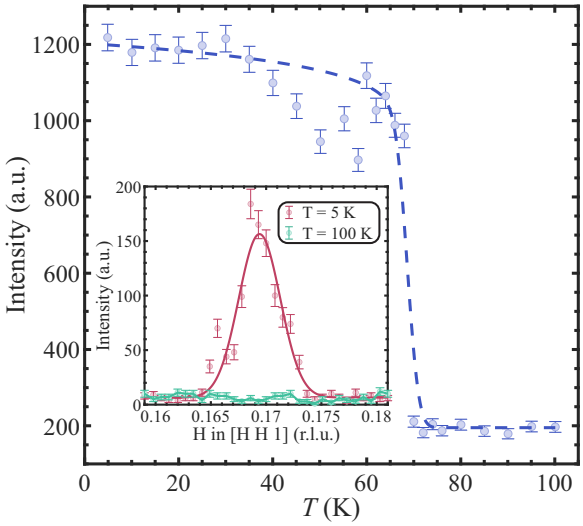

FIG. 4. Integrated intensity as a function of temperature T of the (1/6, 1/6, 1) magnetic peak showing a sharp transition at $T = 70$ K, consistent with specific-heat measurements in Ref. [26], which reveal a first-order transition at $T_N = 70$ K. This indicates that the first-order transition in the heat capacity is associated with the magnetic transition. The dashed line is a guide to the eye. The data near $T_N = 70$ K also indicate a first-order magnetic transition. The inset shows the (1/6, 1/6, 1) peak at $T = 5$ and 100 K. The weak minimum below T_N at ≈50 K does not appear in the specific-heat measurements and is currently not understood.

corrugated honeycomb structure, i.e., the bilayer magnetic structure stacked along the c-axis [Fig. 5(b)]. Throughout, the red sites correspond to one trigonal magnetic sublattice, and the green sites correspond to the other magnetic sublattice. A magnetic model is constructed by assigning a moment along a high-symmetry direction at an origin, for instance, at the lower-left corner, and then successively rotating the spin on the nearest neighbors on the same sublattice clockwise by 60°. The other sublattice is constructed similarly and stacked with antiparallel spins with respect to the first sublattice. See more details on the construction of the magnetic structure in Appendix A. Note that along the [1,0,0] and [0,1,0] directions, the magnetic structure of each sublattice is a cycloid with a 60° turn angle. Thus, for each sublattice, the overall structure is a cycloid with propagation vector $(\eta, \eta, 0)$, with $\eta = 1/6$. Inspection of Fig. 5(b) shows that each hexagon consists of two NN antiparallel pairs and one antiparallel NNN pair, such that the net magnetic moment in each hexagon is zero. Also, note that in this model, all NN spins along the long diagonal are antiparallel.

To model the intensities of the magnetic peaks, I, we use the following equation:

$$I = C|f(Q)|^2 \left| \sum_{j=1}^{k} e^{i\mathbf{Q}\cdot\mathbf{r_j}} \hat{\mathbf{Q}} \times (\hat{\mathbf{m}}_\mathbf{j} \times \hat{\mathbf{Q}}) \right|^2, \tag{1}$$

where C is a scale factor, $\mathbf{Q}$ is the scattering vector, and $\mathbf{r}_j$ and $\hat{\mathbf{m}}_j$ are the position of the Mn moment and the unit vector of the magnetic moment, respectively. $f(Q)$ is the magnetic form factor of Mn^{2+}. Using Eq. (1), the calculated magnetic intensities shown in Fig. 5(c) are in good agreement with the experimental results shown in Fig. 5(a).

The intensity calculations [Eq. (1)] allow us to estimate the average ordered magnetic moment, $\langle gS \rangle$, where $g = 2$ is the spectroscopic-splitting factor, S is the spin quantum number, and μ_B is the Bohr magneton. By comparing nuclear-peak intensities and their structure factors to the observed magnetic-peak intensities, we estimate $\langle gS \rangle \mu_B = 4.2(5)\mu_B$, typical for Mn^{2+} moments.

IV. THEORETICAL DISCUSSION

A. Modeling in terms of a Heisenberg Hamiltonian

We interpret the experimental results in the framework of a two-dimensional J_1-J_2-J_3 Heisenberg model including local anisotropy terms on the honeycomb lattice. We find that this model adequately describes the moments on the puckered-honeycomb Mn^{2+} ions in a single layer of $CaMn_2P_2$. Since moments in different layers order ferromagnetically in the three-dimensional crystal, we focus on a single honeycomb layer in the following. The coupling between the layers could be simply modeled by a ferromagnetic nearest-neighbor exchange J_z, which sets the ordering temperature for weakly coupled layers. Our model of a single honeycomb layer includes NN interactions J_1, NNN J_2, and third-neighbor interactions J_3. We also include single-ion anisotropies D_z and D_{xy} that force the moments to lie within the lattice xy plane ($D_z > 0$), and we introduce a sixfold in-plane anisotropy (D_{xy}), in agreement with the crystalline (point group $\bar{3}m$ or D_{3d}) and time-reversal symmetries. Since the orbital moment of Mn^{2+} vanishes according to Hund's rules, the sixfold anisotropy D_{xy} in $CaMn_2P_2$ is expected to be small. Since the second-neighbor exchange J_2 is expected to be significant in the material [34], and we find that the third-neighbor exchange J_3 affects the required anisotropy D_{xy} for the experimentally observed spiral phase to occur, we include a J_3 term in the Hamiltonian. We find that the most likely range for J_3 is $J_3/J_1 \leqslant 0.1$. We model the spins classically, which is well justified given our experimental observation that $\langle gS \rangle \approx 4.3$. The Hamiltonian reads

$$\begin{aligned} H = {} & J_1 \sum_{\langle n,m \rangle_1} \mathbf{S}_n \cdot \mathbf{S}_m + J_2 \sum_{\langle n,m \rangle_2} \mathbf{S}_n \cdot \mathbf{S}_m \\ & + J_3 \sum_{\langle n,m \rangle_3} \mathbf{S}_n \cdot \mathbf{S}_m + D_z \sum_n (S_n^z)^2 \\ & + \frac{D_{xy}}{2} \sum_n \left[\left(S_n^x + i S_n^y \right)^6 + \text{c.c.} \right], \end{aligned} \tag{2}$$

where $\mathbf{S}_i$ are vectors normalized to $|\mathbf{S}_i| = S$, and n, m denote lattice sites of the honeycomb lattice. The summation over $\langle n, m \rangle_\nu$ runs over each νth-neighbor bond once. The honeycomb lattice is generated by the triangular Bravais lattice vectors $\mathbf{R}_i = i_1\mathbf{a}_1 + i_2\mathbf{a}_2$ with $i_1, i_2 \in \mathbb{Z}$, $\mathbf{a}_1 = (1, 0)$, and $\mathbf{a}_2 = (-\frac{1}{2}, \frac{\sqrt{3}}{2})$. Here, we set the Bravais lattice constant $a_L = 1$. The basis sites are $\delta_A = (0, 0)$ and $\delta_B = (0, 1/\sqrt{3})$ such that the composite index in Eq. (2) reads $n = (i, \alpha)$ with $\alpha = A, B$. The reciprocal-lattice vectors are given by $\mathbf{G}_1 = (2\pi, \frac{2\pi}{\sqrt{3}})$ and $\mathbf{G}_2 = (0, \frac{4\pi}{\sqrt{3}})$, and the first Brillouin zone is depicted in

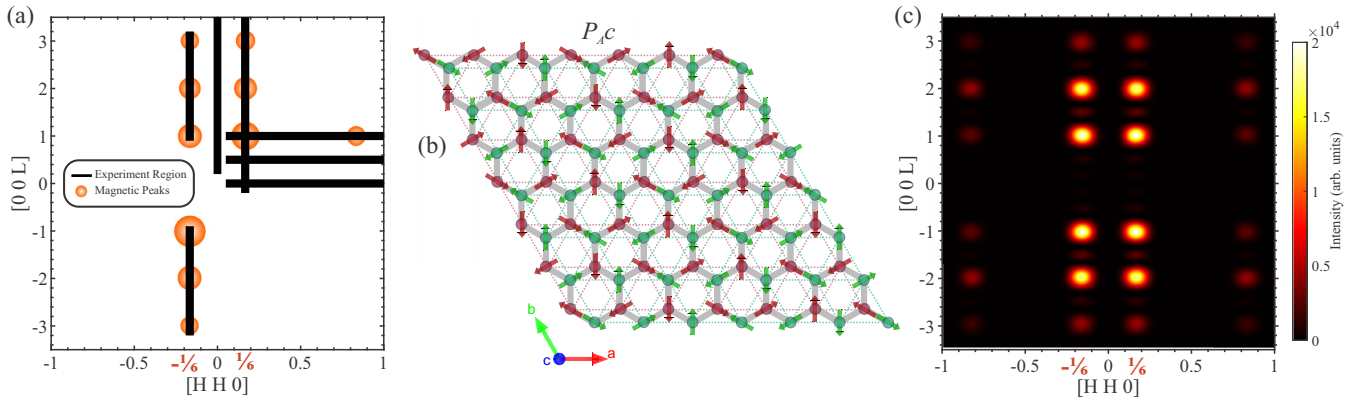

FIG. 5. (a) A compilation of the magnetic reflections observed in the (H, H, L) planes, where the sizes of the spheres roughly reflect observed intensities. Solid black lines show the regions in which the neutron-diffraction experiment was performed. (b) P_AC magnetic model structures [39]. The model structures are constructed by creating a 6×6 in-plane unit cell consisting of the corrugated honeycomb structure. The sites in green correspond to one trigonal layer (magnetic sublattice) and those in red to the other sublattice. More details on the construction of the magnetic structure are provided in Appendix A. (c) Color map of the calculated structure factor based on the magnetic structure shown in (b), which is consistent with the experimental results shown in (a).

Fig. 7(a). To connect to our experimental notation, we write a vector in momentum space as $\mathbf{k} = H\mathbf{G}_1 + K\mathbf{G}_2$ such that the K-point is located at $(H, K) = (\frac{1}{3}, \frac{1}{3})$ (corners of the BZ) and one of the M-points is located at $(H, K) = (0, \frac{1}{2})$ (at the center of the BZ edges).

Next, we analyze the classical ground states of Eq. (2) assuming coplanar magnetic order. The ground-state phase diagram of the J_1-J_2-J_3 Heisenberg model was derived in Refs. [12–14]. A coplanar ground state is in agreement with our experimental data and findings in the literature for the J_1-J_2-J_3 model [12–14]. It can always be favored by a sufficiently large single-ion anisotropy D_z. In the following, we assume $D_z > 0$, corresponding to easy-plane anisotropy, forcing the spins to lie in the ab plane. Following Ref. [15], we parametrize the coplanar spin configuration on the two sublattices as

$$\mathbf{S}_A(\mathbf{R}_i) = S(\sin(\mathbf{Q}\cdot\mathbf{R}_i), \cos(\mathbf{Q}\cdot\mathbf{R}_i)), \tag{3a}$$

$$\mathbf{S}_B(\mathbf{R}_i) = -S(\sin(\mathbf{Q}\cdot\mathbf{R}_i + \phi), \cos(\mathbf{Q}\cdot\mathbf{R}_i + \phi)). \tag{3b}$$

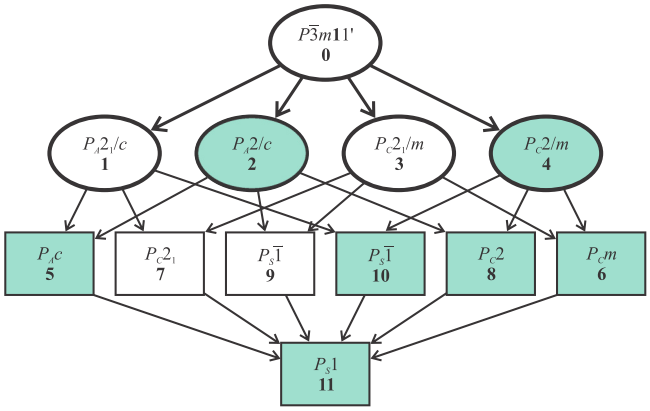

FIG. 6. Allowed magnetic space groups under the crystallographic space group $P\bar{3}m11'$. Magnetic space groups shaded in green are the ones that are consistent with our experimentally observed diffraction patterns [39].

Here, $\phi + \pi$ describes the phase difference between the spins on the A and B sublattices in the same unit cell $\mathbf{R}_i$. Note that Eq. (3b) contains an explicit minus sign such that $\phi = 0$ corresponds to an antiferromagnetic arrangement of A and B spins in the same unit cell. Using this spin parametrization, the classical energy per spin (N = number of spins) reads

$$\begin{aligned}\frac{E}{NS^2} = &-\frac{J_1}{2}[\cos(Q_b - \phi) + \cos(Q_a + Q_b - \phi) - \cos(\phi)] \\ &+ J_2[\cos(Q_a) + \cos(Q_b) + \cos(Q_a + Q_b)] \\ &- \frac{J_3}{2}[\cos(Q_a + 2Q_b - \phi) + \cos(Q_a)\cos(\phi)].\end{aligned} \tag{4}$$

Here, $Q_a = \mathbf{Q}\cdot\mathbf{a}_1$ and $Q_b = \mathbf{Q}\cdot\mathbf{a}_2$ such that $\mathbf{Q} = H\mathbf{G}_1 + K\mathbf{G}_2 = \frac{Q_a}{2\pi}\mathbf{G}_1 + \frac{Q_b}{2\pi}\mathbf{G}_2$. We can analytically find the classical ground-state energy from the conditions

$$\frac{\partial E}{\partial Q_a} = \frac{\partial E}{\partial Q_b} = \frac{\partial E}{\partial \phi} = 0. \tag{5}$$

Let us first discuss the case of $J_3 = D_{xy} = 0$. Then, the ground state exhibits a continuous degeneracy of spiral states with wavevectors $\mathbf{Q} = (Q_a, Q_b)$ that fulfill [15]

$$\cos(Q_a) + \cos(Q_b) + \cos(Q_a + Q_b) = \frac{1}{2}\left(\frac{J_1^2}{4J_2^2} - 3\right). \tag{6}$$

The phase difference ϕ is determined by

$$\sin(\phi) = 2J_2[\sin(Q_b) + \sin(Q_a + Q_b)]. \tag{7}$$

For $\frac{1}{6} < J_2/J_1 < \frac{1}{2}$, the manifold of degenerate wavevectors forms a circle around the Γ point, as shown in Fig. 7(a) for $J_2/J_1 = 0.25$. The radius of the circle increases continuously with increasing J_2. For $J_2/J_1 > 0.5$, the degenerate states are located around the K and K' points, which they approach in the large-J_2 limit [15]. We refer to Appendix C for a detailed derivation of these results. In $CaMn_2P_2$ we find the propagation vector $(H, K) = (\frac{1}{6}, \frac{1}{6})$, which lies along the Γ-K direction and corresponds to one of the degenerate states for $J_2/J_1 = 0.25$. This regime of large frustration is thus relevant for $CaMn_2P_2$ and will be our focus in the following.

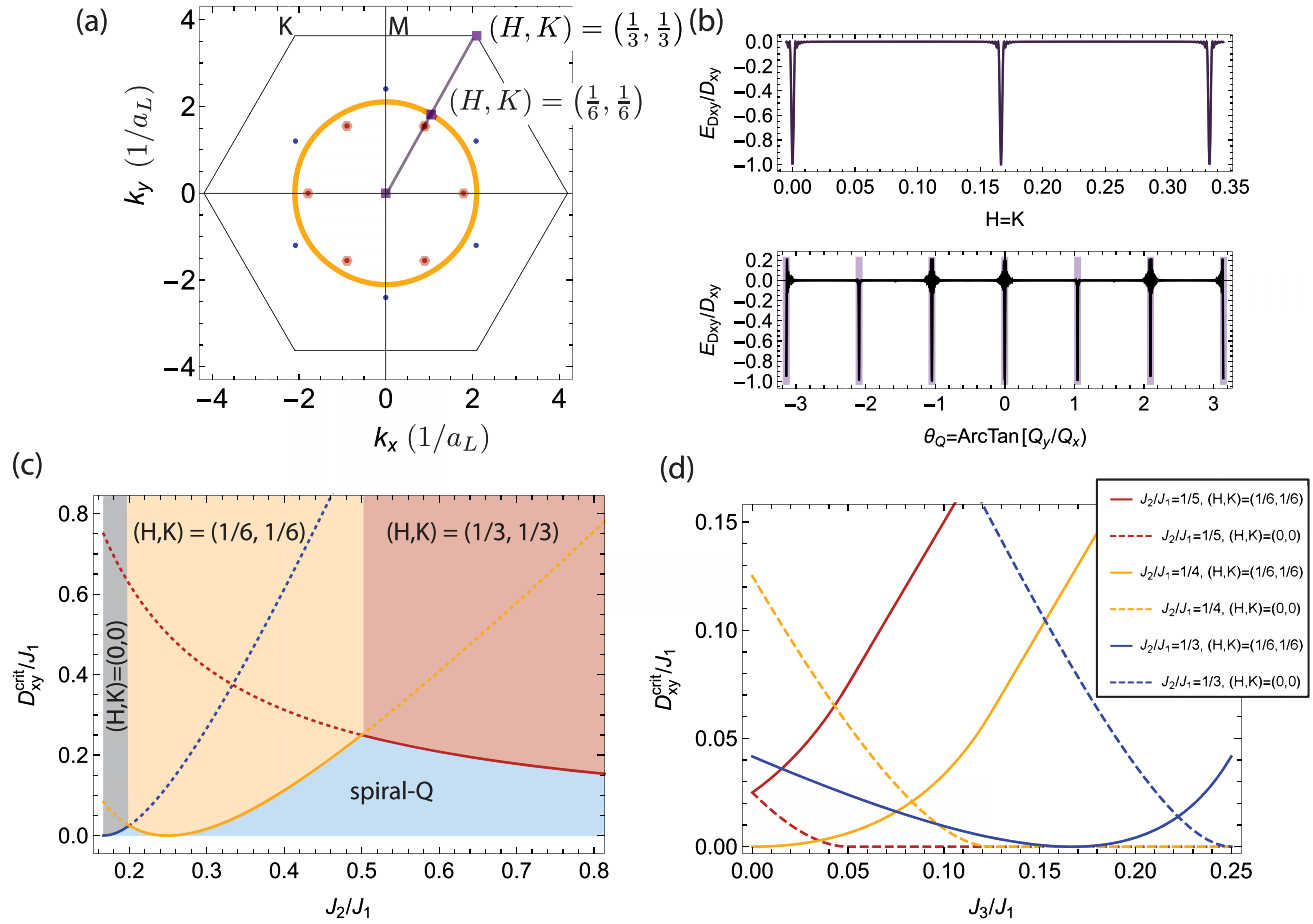

FIG. 7. (a) Manifold of wavevectors (k_x, k_y) of spiral magnetic ground states in the J_1-J_2-J_3 Heisenberg model for $J_2/J_1 = 0.25$. Different colors correspond to different values of J_3: $J_3 = 0$ (yellow), AFM $J_3/J_1 = 0.05$ (red hexagons), and FM $J_3/J_1 = -0.05$ (blue dots). Sixfold anisotropy D_{xy} favors wavevectors shown as purple squares (as well as symmetry-related ones). (b) The upper panel shows sixfold anisotropy energy $E_{D_{xy}}$ of single-Q magnetic spirals with $H = K$ along a path from the origin to K [shown in panel (a)]. Anisotropy favors spirals with $H = K = 0$ (Néel order), $H = K = \frac{1}{6}$, and $H = K = \frac{1}{3}$. The lower panel shows $E_{D_{xy}}$ of single-Q magnetic spirals along the yellow circle in (a) as a function of polar angle. Anisotropy favors $H = K = \frac{1}{6}$ and symmetry-related wavevectors obtained by 60° rotations. (c) Magnetic ground-state phase diagram of the J_1-J_2-D_{xy} Heisenberg model as a function of J_2 and D_{xy} for fixed $J_1 = 1$ and $J_3 = 0$. The solid and dashed lines denote critical D_{xy}^{crit} that favor commensurate states with $(H, K) = (0, 0)$ (blue), $(H, K) = (\frac{1}{6}, \frac{1}{6})$ (yellow), and $(H, K) = (1/3, 1/3)$ (red) over spirals with other wavevectors. The experimentally observed $(H, K) = (\frac{1}{6}, \frac{1}{6})$ spiral phase extends from $0.2 \leqslant J_2/J_1 \leqslant 0.5$, and the critical value of D_{xy} exhibits a minimum of zero at $J_2/J_1 = 0.25$. (d) The critical value of the sixfold anisotropy D_{xy}^{crit} as a function of J_3 required to favor commensurate spirals with $(H, K) = (\frac{1}{6}, \frac{1}{6})$ (solid) or $(H, K) = (0, 0)$ (dashed). Nonzero J_3 moves the ground-state wavevector Q closer to the origin, resulting in monotonously decreasing dashed lines. D_{xy}^{crit} for $(H, K) = (\frac{1}{6}, \frac{1}{6})$ (solid) decreases if J_3 moves Q closer to $(\frac{1}{6}, \frac{1}{6})$ (see $J_2/J_1 = 1/3$), and it increases otherwise (see $J_2/J_1 = 0, 1/4$).

Nonzero J_3 selects a discrete subset of six wavevectors for the ground-state spin configuration. For AFM $J_3 > 0$ these lie along the Γ-K (and symmetry-related) directions in the Brillouin zone [see the red hexagons in Fig. 7(a)]. In contrast, for FM $J_3 < 0$ these lie along the Γ-M direction for $J_2/J_1 < 1/2$ [see the blue dots in Fig. 7(a)] and along the K-M line for $1/2 < J_2/J_1 < 1$ (not shown). The wavevectors shown in Fig. 7(a) are for AFM $J_3/J_1 = 0.05$ (red hexagons) and for FM $J_3/J_1 = -0.05$ (blue circles). Since AFM J_3 favors Néel order, which is described by $(H, K) = (0, 0)$ and $\phi = 0$, the red wavevectors move towards the Γ point with increasing AFM J_3. In contrast, with increasing FM $J_3 < 0$ (i.e., more negative values), they move towards the M point. We note that quantum and thermal fluctuations also select six discrete wavevectors, which correspond to the ones favored by FM J_3 [15]. We therefore conclude that the experimentally observed wavevector $(H, K) = (\frac{1}{6}, \frac{1}{6})$ is consistent with AFM $J_3 > 0$. In contrast, it is not favored by FM J_3 and it is also not selected via an order-by-disorder mechanism.

We now analyze the effect of a local sixfold single-ion anisotropy term whose strength is parametrized by D_{xy} [see Eq. (2)]. As shown in Fig. 7(b), nonzero D_{xy} favors a discrete number of spiral states, which are consistent with an alignment of spins along one of the six high-symmetry directions on every site. Moving along the direction $H = K$ in the Brillouin zone, we find that D_{xy} equally favors Néel order ($H = K = 0$), the experimentally observed spiral order with $H = K = \frac{1}{6}$, and a shorter spiral with wavevector

$H = K = \frac{1}{3}$ (K-point). These three wavevectors are also highlighted in Fig. 7(a) as purple squares. In addition to these three wavevectors, D_{xy} also favors symmetry-related wavevectors as shown in the lower panel of Fig. 7(b), which are obtained by 60° rotations. In Fig. 7(c), we show that a magnetic spiral with the experimentally observed wavevector $(H, K) = (\frac{1}{6}, \frac{1}{6})$ is stabilized over a wide region of J_2/J_1 and D_{xy}. Specifically, for $0.2 < J_2/J_1 < 0.5$ and $J_3 = 0$, the system enters a magnetic spiral with $H = K = \frac{1}{6}$ at a critical value of D_{xy}^{crit} (yellow region). The critical value D_{xy}^{crit} is a convex function of J_2/J_1 and exhibits a minimum of zero at $J_2/J_1 = 0.25$. For smaller values of $J_2/J_1 < 0.2$, the sixfold anisotropy drives the system into a Néel-ordered phase instead (gray region), while for larger values of $J_2/J_1 > 0.5$, it will transition into a magnetic spiral with $H = K = \frac{1}{3}$ (red region). For nonzero AFM J_3 the Néel phase extends until larger values of J_2/J_1, which sets a limit to the size of J_3/J_1 in $CaMn_2P_2$.

To study the dependence on J_3/J_1 more systematically, we plot in Fig. 7(d) the evolution of D_{xy}^{crit} as a function of AFM J_3/J_1 for several fixed values of J_2/J_1. We focus on the region of $J_2/J_1 < 0.5$, where the Néel-ordered phase competes with the $H = K = \frac{1}{6}$ phase. First, we find that the behavior of $D_{xy}^{\text{crit},1/6}$ (solid lines) depends on the value of J_2/J_1. Since increasing J_3 moves the minimum-energy spiral wavevector towards the Γ point, J_3 reduces $D_{xy}^{\text{crit},1/6}$ for $J_2/J_1 > 1/4$, but increases it for $J_2/J_1 < 1/4$. Second, since J_3 favors the Néel ordered state over the spiral, we observe that increasing J_3 generally reduces the critical value $D_{xy}^{\text{crit,Néel}}$ needed to stabilize the Néel phase (dashed lines). The dashed lines are thus monotonously decreasing as a function of J_3. For a given value of J_2/J_1, we thus find that $D_{xy}^{\text{crit,Néel}} < D_{xy}^{\text{crit},1/6}$ for sufficiently large J_3 such that the sixfold anisotropy drives the system into the Néel phase. The position of the crossing point between solid and dashed lines in Fig. 7(d) increases with increasing J_2/J_1, which is a result of the minimum-energy wavevector lying closer to $H = K = \frac{1}{6}$ than to the origin [see Fig. 7(a)].

We conclude from this analysis that when $0.2 < J_2/J_1 < 0.5$, the presence of a sixfold anisotropy D_{xy} is sufficient to stabilize the $H = K = \frac{1}{6}$ spiral order even without a third-neighbor interaction term J_3. The required value of D_{xy} to drive the system from an incommensurate spiral into the commensurate $H = K = \frac{1}{6}$ spiral phase vanishes at $J_2/J_1 = 0.25$ and remains small in the vicinity of this point. Regarding the effect of nonzero J_3, we find that AFM J_3 selects a wavevector along the observed $H = K$ direction, while FM J_3 selects different wavevectors that are at 30°-rotated directions in the Brillouin zone. An AFM third-neighbor interaction is thus more consistent with our experimental findings than a FM one. Since AFM J_3 also favors the Néel state, the minimum-energy spiral wavevector $\mathbf{Q}$ moves towards the origin with increasing J_3. For large $J_2/J_1 > 0.5$, where the wavevector lies between the $(\frac{1}{6}, \frac{1}{6})$ and the K point, this moves $\mathbf{Q}$ closer to $(\frac{1}{6}, \frac{1}{6})$ and thus reduces the value of D_{xy} necessary to enter the commensurate $H = K = \frac{1}{6}$ spiral phase [see the blue line in Fig. 7(d)]. For smaller values of J_2/J_1, a larger value of J_3 drives the system into the Néel phase and can thus be excluded for $CaMn_2P_2$. To summarize, the most likely parameter range describing $CaMn_2P_2$ is $J_2/J_1 \approx 0.25$–0.4, $J_3/J_1 \lesssim 0.1$, and $D_{xy} > D_{xy}^{\text{crit}} \approx 0$–$0.1J_1$. Further experimental work, such as, e.g., inelastic neutron scattering results, is needed to determine the values of the exchange and anisotropy parameters more precisely.

B. Emergent Potts-nematic order and first-order phase transition

The frustration-induced spiral magnetic order that we observe in $CaMn_2P_2$ leads to the emergence of a Potts-nematic order parameter. This composite order parameter is bilinear in the spins and involves their scalar product on nearest-neighbor sites:

$$\psi(\mathbf{R}) = \mathbf{S}_A(\mathbf{R}) \cdot \mathbf{S}_B(\mathbf{R}) + e^{-\frac{2\pi i}{3}} \mathbf{S}_A(\mathbf{R}) \cdot \mathbf{S}_B(\mathbf{R} - \mathbf{a}_2) + e^{-\frac{4\pi i}{3}} \mathbf{S}_A(\mathbf{R}) \cdot \mathbf{S}_B(\mathbf{R} - \mathbf{a}_1 - \mathbf{a}_2). \quad (8)$$

This complex bond order parameter is finite and translationally invariant in any of the three spiral magnetic states with $(H, K) = \{\mathbf{Q}_1, \mathbf{Q}_2, \mathbf{Q}_3\} = (\frac{1}{6}, \frac{1}{6}), (-\frac{1}{3}, \frac{1}{6}), (\frac{1}{6}, -\frac{1}{3})$. In Fig. 8, we show the three degenerate ground states of the J_1-J_2-J_3-D_{xy} Heisenberg model in the regime where $D_{xy} > D_{xy,\text{crit}}$ and $0.2 < J_2/J_1 < 0.5$ [see Fig. 7(c)]. When placed on the Mn ions in $CaMn_2P_2$, this magnetic structure corresponds to magnetic space group (MSG) P_S1, which is one of the MSGs that are consistent with experiment (see Fig. 6). The related magnetic structure for $D_{xy} < 0$, for which the spin at the origin (yellow circle) is rotated by $\frac{\pi}{2}$, lies in the MSG P_Cm that is also consistent with the experimental data. The three panels in Fig. 8 depict the symmetry-related states with propagation vectors $\mathbf{Q}_i$, and the insets show the value of the spatially homogeneous complex Potts-nematic order parameter, whose argument follows the direction of the ordering wavevector. It is a generalization of the Ising nematic bond order parameter known to underlie the tetragonal to orthorhombic transition via magnetoelastic couplings that is observed in tetragonal iron-based arsenides such as $CaFe_2As_2$ [40,41].

Under a threefold rotation around an A site, the Potts-nematic order parameter transforms as $\psi \xrightarrow{C_3} \exp(\frac{2\pi i}{3})\psi$. Under a mirror operation m_{yz} that sends $x \to -x$, it transforms as $\psi \xrightarrow{m_{yz}} \psi^*$. Its finite-temperature behavior is thus described by the Landau-Ginzburg free-energy functional of a three-state Potts model [15]. In three dimensions this analysis predicts a first-order phase transition into a state with long-range Potts order due to a symmetry-allowed third-order term. This is also in agreement with Monte Carlo simulations [42]. The emergence of long-range Potts-nematic order can therefore naturally account for the experimentally observed first-order magnetic phase transition in $CaMn_2P_2$. Note that different honeycomb layers are ordered ferromagnetically along the c direction in $CaMn_2P_2$, corresponding to an ordering wavevector with integer L, where $\mathbf{Q} = (H, K, L)$. Since ψ is a composite magnetic order parameter, it is strongly intertwined with magnetism, and the discontinuous development of long-range Potts order at the first-order transition can thus uplift the magnetic transition to occur as a joint first-order transition. The system then simultaneously develops long-range Potts-nematic and magnetic order. Such a behavior is known to occur, for example, in the triangular lattice

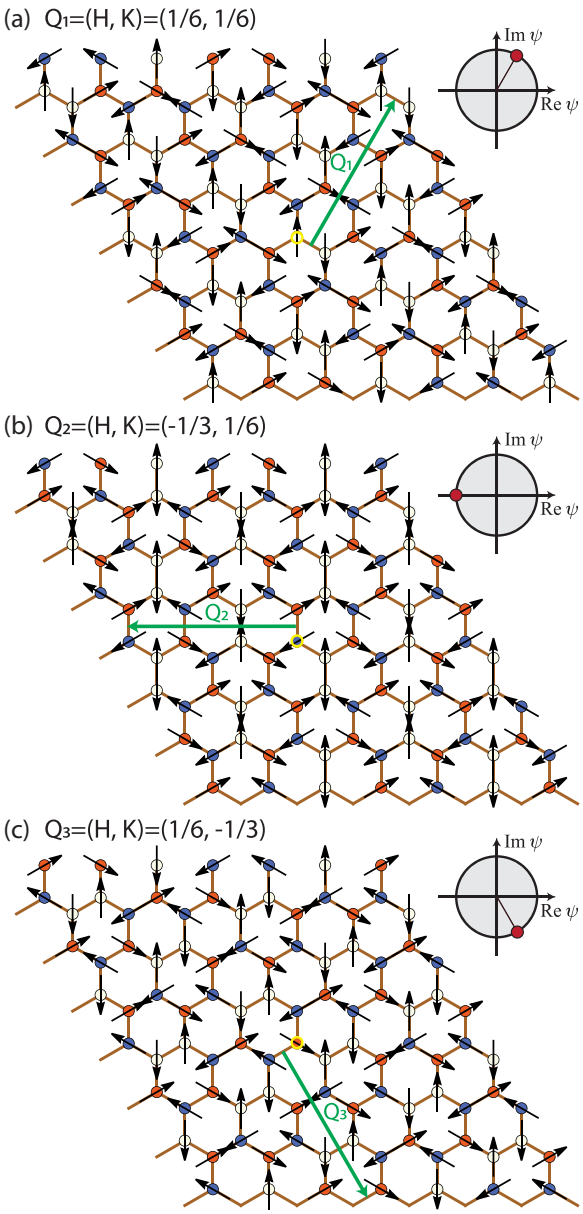

FIG. 8. Panels (a), (b), and (c) show the three degenerate ground states $(H, K) = (\frac{1}{6}, \frac{1}{6}), (-\frac{1}{3}, \frac{1}{6}), (\frac{1}{6}, -\frac{1}{3})$ of the J_1-J_2-D_{xy} Heisenberg model for $D_{xy} > 0$. In each panel, the bond order parameter $\psi(\mathbf{R})$ is invariant under translations, but different panels describe different bond orders: the antiparallel nearest-neighbor spin pair occurs along three different bonds in the three panels (a)–(c). The complex argument of ψ is given by the polar angle of the corresponding wavevector $\mathbf{Q}_i$ in the Brillouin zone (see the red hexagons in Fig. 7).

antiferromagnet $Fe_{1/3}NbSe_2$ [36]. This can also explain why the related compounds $CaMn_2Pn_2$ with Pn = Sb, Bi that exhibit Néel order, for which such a three-state Potts-nematic order is absent, develop magnetic order via a continuous phase transition.

Since long-range Potts-nematic order breaks the threefold rotational symmetry of the lattice, we predict the emergence of three lattice distortion domains due to a finite magnetoelastic coupling. The domains are characterized by different values of the Potts-nematic order parameter ψ, as shown in Fig. 8. However, the coupling between magnetic and lattice degrees of freedom is expected to be small in this system, since the orbital moment of the magnetic ions Mn^{2+} vanishes according to Hund's rules, and spin-orbit coupling is therefore small. This could be the reason why lattice distortion and crystal symmetry lowering could not be detected in previous x-ray diffraction studies [26]. An alternative explanation is the emergence of a complex multi-Q magnetic order that preserves all lattice symmetries. It is worth noting, however, that Raman scattering studies have reported the appearance of additional peaks when going from the paramagnetic phase at room temperature to the magnetic phase at $T < T_N$ [43]. Further investigations of the effects of magnetic ordering on the lattice and its excitations are needed to address these open questions. We emphasize that magnetic spiral-Q order with a single finite-momentum wavevector breaks threefold rotation symmetry via selection of one of the three symmetry-equivalent propagation vectors $\mathbf{Q}_i$. In the single-Q spiral state, we thus expect the appearance of three magnetic domains characterized by different magnetic propagation vectors in the magnetically ordered state.

V. CONCLUSIONS

Using neutron-diffraction measurements, we find that $CaMn_2P_2$ undergoes a first-order antiferromagnetic transition at $T_N = 70(1)$ K into a state with a 6×6 times enlarged magnetic unit cell. The average ordered magnetic moment is $\langle gS \rangle \mu_B = 4.2(5)\mu_B$. The integrated intensity of the major $(H, K, L) = (\frac{1}{6}, \frac{1}{6}, 1)$ magnetic peak versus temperature shows an abrupt decrease at T_N that is a characteristic of a first-order phase transition. Focusing on the experimentally discovered ground state, we interpret these results using a frustrated J_1-J_2-J_3 Heisenberg model with easy-plane anisotropy D_z and a sixfold in-plane anisotropy D_{xy}, and we show that this propagation wavevector signals the presence of a substantial degree of frustration. We relate the appearance of the first-order magnetic transition to a composite three-state Potts-nematic bond order parameter that simultaneously develops long-range order and drives the magnetic transition to become first-order. Based on our analysis, we predict the emergence of three symmetry-related magnetic and lattice distortion domains that deserve further studies.

ACKNOWLEDGMENTS

This research was supported by the U.S. Department of Energy, Office of Basic Energy Sciences, Division of Materials Sciences and Engineering. Ames National Laboratory is operated for the U.S. Department of Energy by Iowa State University under Contract No. DE-AC02-07CH11358.

APPENDIX A: CONSTRUCTING THE MAGNETIC STRUCTURE

We describe the proposed magnetic structures with space group P_Ac, shown in Fig. 5(b) in the main text. The

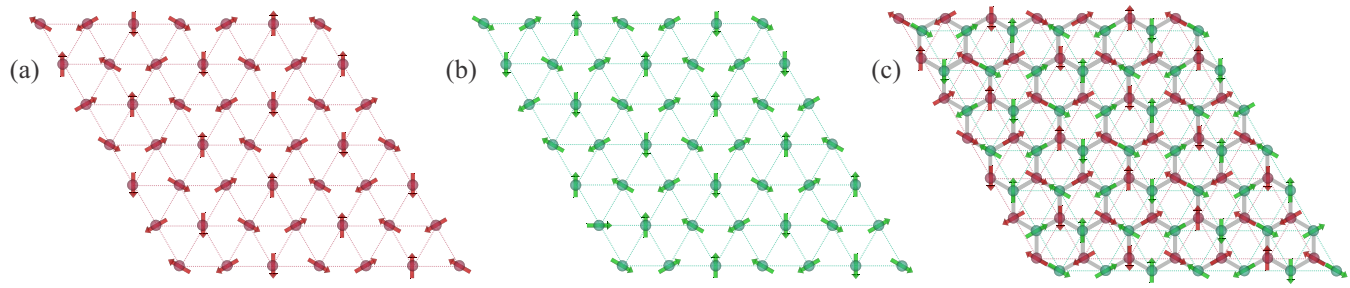

FIG. 9. Parts (a) and (b) depict the 6×6 in-plane trigonal sublattices that form the honeycomb structure. In (a), we assign a spin along a high-symmetry direction at the origin (lower-left corner), and the nearest neighbors along the a- and b-axes are successively rotated by a 60° angle in the clockwise direction to create the sublattice. The sublattice shown in (b) is constructed by flipping the spin direction at the origin (lower-left corner) with respect to the one in the origin of (a), and the nearest neighbors along the a- and b-axes are successively rotated by a 60° angle in the clockwise direction. (c) The corrugated honeycomb structure with magnetic spacegroup P_Ac is constructed by stacking the sublattices shown in (a) and (b).

magnetic structure is constructed by generating two 6×6 in-plane trigonal sublattices that are stacked together to form the honeycomb structure. In Fig. 9(a), the trigonal sublattice is constructed by assigning a spin at the origin (lower-left corner) pointed along one of the high-symmetry directions, and successively rotating the nearest neighbors in the a- and b-directions by a 60° angle in the counterclockwise direction. In Fig. 9(b) we construct the other trigonal sublattice for magnetic structure. The spin at the origin (lower-left corner) is flipped with respect to the spin at the origin of the trigonal sublattice depicted in Fig. 9(a). The nearest neighbors along the a and b directions are rotated successively by a 60° angle in the counterclockwise direction, the same way as before, to construct the other sublattice. The magnetic structure with spacegroup P_Ac is formed by stacking the trigonal sublattice shown in Fig. 9(b) on the trigonal sublattice shown in Fig. 9(a) to form the corrugated honeycomb lattice, as depicted in Fig. 9(c).

APPENDIX B: SYSTEMATICALLY SEARCHING OTHER MAGNETIC STRUCTURES

We emphasize that the magnetic structure shown in Fig. 5(b) of the main text with magnetic space group P_Ac [39] is not unique with respect to the neutron-diffraction data. Systematically searching through the Symmetry-Based Computational Tools for Magnetic Crystallography [39] (Fig. 6 in the main text), we find a few more magnetic structures shown in Fig. 10 that are consistent with the peak positions in the diffraction measurements. The Bilbao crystallographic database allows for other magnetic structures with the propagation vector of (1/6, 1/6, 0), as shown in Fig. 11; however, the intensity calculations are inconsistent with the experimental observations. In particular, these configurations show intensities at $(\pm 1/6, \pm 1/6, 0)$, which are not observed experimentally. We note that when constructing the magnetic structure using the Bilbao database, we assume that the spin direction at the origin is a high-symmetry direction, and we rotate nearest-neighbor moments in the same sublattice by 60°. For simplicity, we divide the rotation between the spin at the origin and the edge by 6, i.e., 360°/6.

APPENDIX C: DETAILS OF GROUND-STATE ANALYSIS OF A SPIN HAMILTONIAN

The honeycomb lattice is generated by the Bravais lattice vectors

$$\mathbf{a}_1 = (1, 0), \tag{C1}$$

$$\mathbf{a}_2 = \left(\cos\frac{2\pi}{3}, \sin\frac{2\pi}{3}\right) = \left(-\frac{1}{2}, \frac{\sqrt{3}}{2}\right). \tag{C2}$$

A Bravais lattice vector is given by $R_i = i_1\mathbf{a}_1 + i_2\mathbf{a}_2$ with $i_1, i_2 \in \mathbb{Z}$. Here, we have set the Bravais lattice constant to 1. The honeycomb model has two atoms (or spins) per unit cell. The basis vectors are given by $\mathbf{b}_A = (0, 0)$ and $\mathbf{b}_B = (0, \frac{1}{\sqrt{3}})$.

Our choice of $\mathbf{a}_i$ leads to the reciprocal-lattice vectors $\mathbf{G}_i \cdot \mathbf{a}_j = 2\pi\delta_{ij}$ being given by

$$\mathbf{G}_1 = \left(2\pi, \frac{2\pi}{\sqrt{3}}\right), \tag{C3}$$

$$\mathbf{G}_2 = \left(0, \frac{4\pi}{\sqrt{3}}\right). \tag{C4}$$

For later reference, we introduce the notation $\mathbf{k} = H\mathbf{G}_1 + K\mathbf{G}_2$. The K point in the Brillouin Zone is located at $(H, K) = (\frac{1}{3}, \frac{1}{3})$ or $\mathbf{k} = (\frac{2\pi}{3}, \frac{2\pi}{\sqrt{3}})$ and the M point is located at $(H, K) = (0, \frac{1}{2})$ or $\mathbf{k} = (0, \frac{2\pi}{\sqrt{3}})$.

The Hamiltonian of the classical J_1-J_2-J_3 Heisenberg model on the honeycomb lattice then reads

$$\begin{aligned} H = {} & J_1 \sum_{R_i} \sum_{\delta_i^{(1)}=\delta_1^{(1)}}^{\delta_3^{(1)}} \mathbf{S}_A(R_i) \cdot \mathbf{S}_B\left(R_i + \delta_i^{(1)}\right) \\ & + \frac{J_2}{2} \sum_{R_i} \sum_{\delta_i^{(2)}=\delta_1^{(2)}}^{\delta_6^{(2)}} \left[\mathbf{S}_A(R_i) \cdot \mathbf{S}_A\left(R_i + \delta_i^{(2)}\right)\right. \\ & \left. + \mathbf{S}_B(R_i) \cdot \mathbf{S}_B\left(R_i + \delta_i^{(2)}\right)\right] \\ & + J_3 \sum_{R_i} \sum_{\delta_i^{(3)}=\delta_1^{(3)}}^{\delta_3^{(3)}} \mathbf{S}_A(R_i) \cdot \mathbf{S}_B\left(R_i + \delta_i^{(3)}\right). \end{aligned} \tag{C5}$$

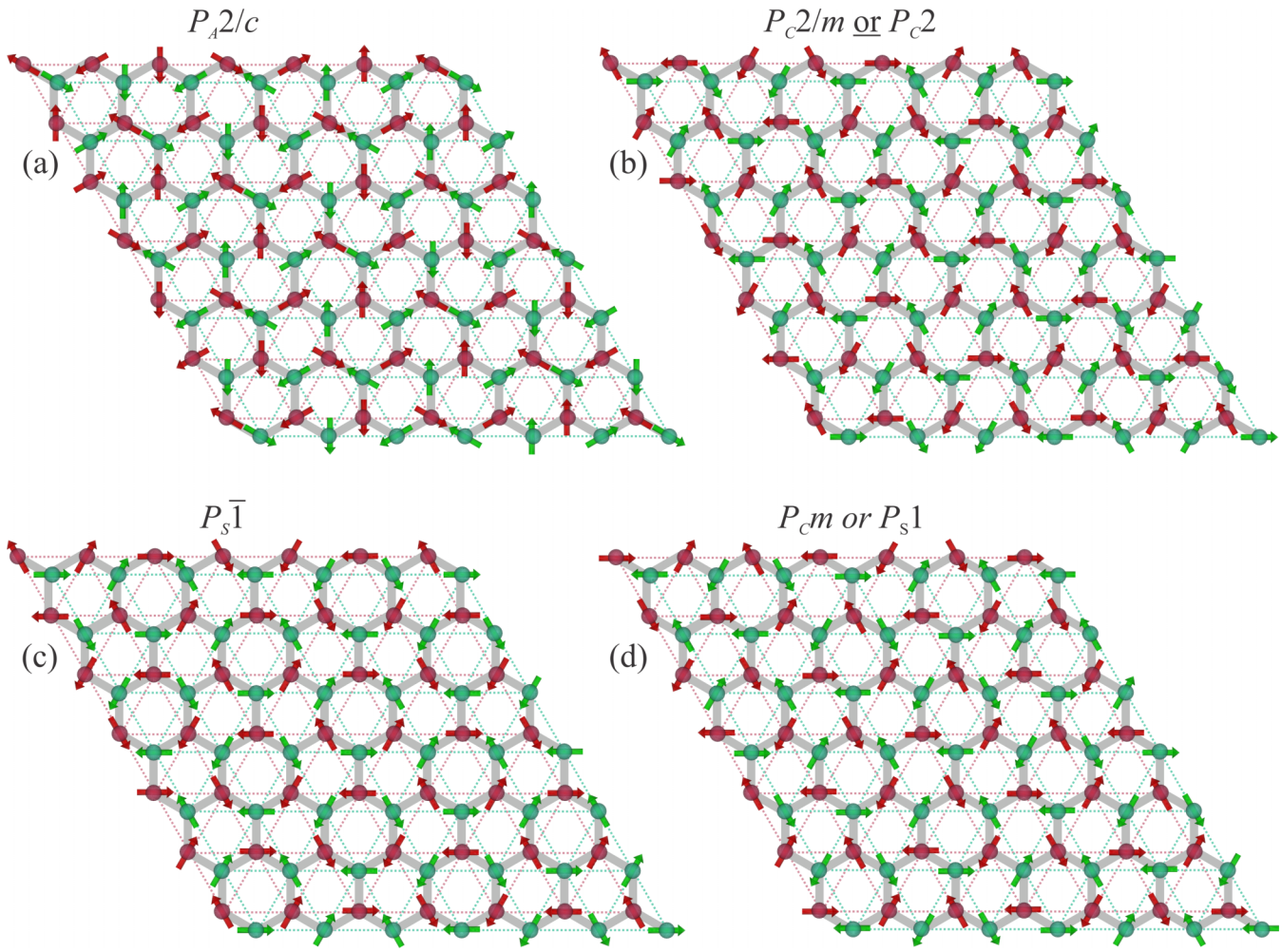

FIG. 10. Illustration of possible magnetic structures allowed by the Bilbao magnetic spacegroups [39] with calculated intensities consistent with the experimental observation. Calculated intensities for these configurations are similar to the one shown in the main text for the P_Ac magnetic space group.

The set of first, second, and third (Bravais) neighbors reads

$$\left\{\delta_i^{(1)}\right\} = \{(0,0), -\mathbf{a}_1 - \mathbf{a}_2, -\mathbf{a}_2\}, \tag{C6}$$

$$\left\{\delta_i^{(2)}\right\} = \{\mathbf{a}_1, \mathbf{a}_1 + \mathbf{a}_2, \mathbf{a}_2, -\mathbf{a}_1, -\mathbf{a}_1 - \mathbf{a}_2, -\mathbf{a}_2\}, \tag{C7}$$

$$\left\{\delta_i^{(3)}\right\} = \{\mathbf{a}_1, -\mathbf{a}_1, -\mathbf{a}_1 - 2\mathbf{a}_2\}. \tag{C8}$$

Following Ref. [15], we parametrize the ground state in the following way:

$$\mathbf{S}_A(R_i) = S(\sin(\mathbf{Q}\cdot R_i), \cos(\mathbf{Q}\cdot R_i)), \tag{C9}$$

$$\mathbf{S}_B(R_i) = -S(\sin(\mathbf{Q}\cdot R_i + \phi), \cos(\mathbf{Q}\cdot R_i + \phi)). \tag{C10}$$

We often write

$$\mathbf{Q} = H\mathbf{G}_1 + K\mathbf{G}_2 = \frac{Q_a}{2\pi}\mathbf{G}_1 + \frac{Q_b}{2\pi}\mathbf{G}_2, \tag{C11}$$

where it also holds that $Q_a = \mathbf{Q}\cdot\mathbf{a}_1$ and $Q_b = \mathbf{Q}\cdot\mathbf{a}_2$.

The classical energy per spin (N = number of spins) using this spin parametrization reads

$$\begin{aligned}\frac{E(\mathbf{Q},\phi)}{NS^2} = &-\frac{J_1}{2}[\cos(Q_b-\phi) \\ &+ \cos(Q_a+Q_b-\phi) - \cos(\phi)] \\ &+ J_2[\cos(Q_a) + \cos(Q_b) + \cos(Q_a+Q_b)] \\ &- J_3\Big[\frac{1}{2}\cos(Q_a-\phi) \\ &+ \cos(Q_a+Q_b)\cos(Q_b-\phi)\Big].\end{aligned} \tag{C12}$$

The J_3 term can also be written as

$$-\frac{J_3}{2}[\cos(Q_a+2Q_b-\phi) + \cos(Q_a)\cos(\phi)]. \tag{C13}$$

We can analytically find the minimum energy, which equals the classical ground-state energy, via

$$\frac{\partial E}{\partial Q_a} = \frac{\partial E}{\partial Q_b} = \frac{\partial E}{\partial \phi} = 0. \tag{C14}$$

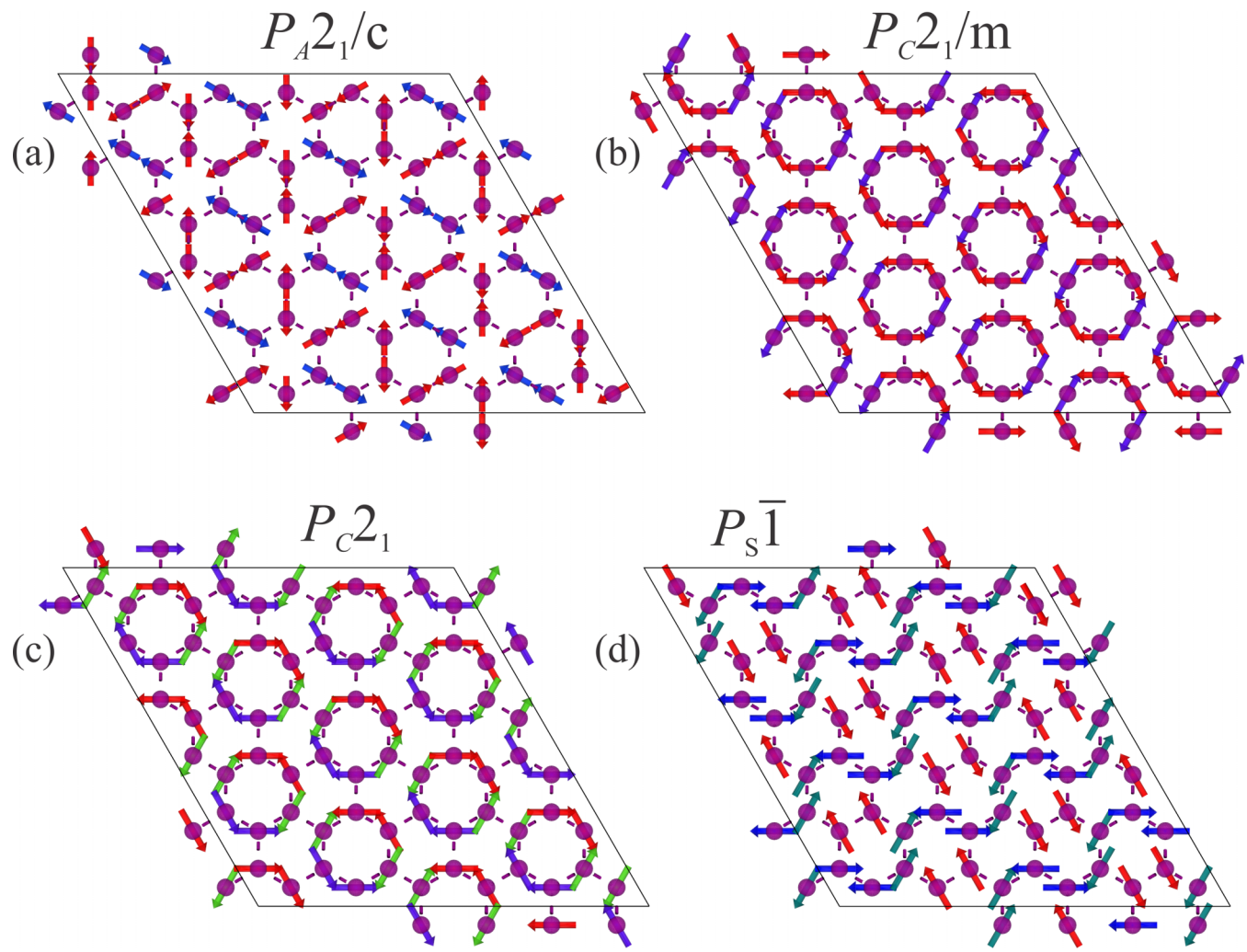

FIG. 11. Illustration of possible magnetic structures allowed by the Bilbao magnetic spacegroups [39] with calculated intensities inconsistent with the experimental observation. In particular, these configurations show intensities at $(\pm 1/6, \pm 1/6, 0)$, which are not observed experimentally [see Figs. 3(b) and 3(c)].

Numerically, it is advantageous to directly minimize $E(Q_a, Q_b, \phi)$ for different random starting points of $0 \leqslant Q_a, Q_b < 2\pi$ and $0 \leqslant \phi < 2\pi$.

1. Case of $J_3 = 0$

Let us first consider the case of $J_3 = 0$. Here, we find from $\frac{\partial E}{\partial Q_a} = \frac{\partial E}{\partial Q_b} = \frac{\partial E}{\partial \phi} = 0$ the set of equations

$$2J_2[\sin(Q_a) + \sin(Q_a + Q_b)] = \sin(Q_a + Q_b - \phi), \quad \text{(C15)}$$

$$2J_2[\sin(Q_b) + \sin(Q_a + Q_b)] = \sin(Q_b - \phi) + \sin(Q_a + Q_b - \phi), \quad \text{(C16)}$$

$$\sin(Q_b - \phi) + \sin(Q_a + Q_b - \phi) = \sin(\phi). \quad \text{(C17)}$$

Here, we have set $J_1 = 1$ and thus $J_2 \equiv J_2/J_1$. Inserting the third equation into the second one yields

$$\sin(\phi) = 2J_2[\sin(Q_b) + \sin(Q_a + Q_b)]. \quad \text{(C18)}$$

The first equation then becomes

$$2J_2[\sin(Q_a) + \sin(Q_a + Q_b)] = \sin(Q_a + Q_b - \phi) \quad \text{(C19)}$$

$$= \sin(Q_q + Q_b)\cos(\phi) - \cos(Q_a + Q_b)\sin(\phi) \quad \text{(C20)}$$

$$= \sin(Q_q + Q_b)\cos(\phi) - 2J_2\cos(Q_a + Q_b)[\sin(Q_b) + \sin(Q_a + Q_b)]. \quad \text{(C21)}$$

Solving for $\cos(\phi)$ and using that

$$\frac{\sin(Q_a) + \cos(Q_a + Q_b)\sin(Q_b)}{\sin(Q_a + Q_b)} = \cos(Q_b), \quad \text{(C22)}$$

we arrive at

$$\cos(\phi) = 2J_2[1 + \cos(Q_b) + \cos(Q_a + Q_b)]. \quad \text{(C23)}$$

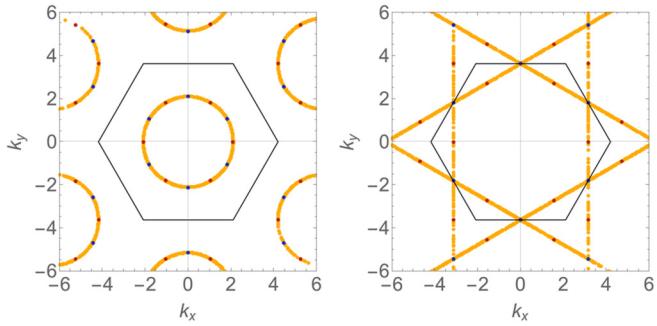

FIG. 12. Manifold of wavevectors (k_x, k_y) (in units of $1/a_L$) of spiral magnetic ground states in the J_1-J_2-J_3 Heisenberg model for $J_2/J_1 = 0.25$ (left) and $J_2/J_1 = 0.5$ (right). Different colors correspond to different values of J3. Specifically, $J_3 = 0$ (yellow); AFM $J_3/J_1 = 10^{-3}$ (red); and FM $J_3/J_1 = -10^{-3}$ (blue). The black hexagon shows the first Brillouin zone. Note that nonzero J_3 selects six symmetry-related wavevectors, while there exists a continuous manifold of degenerate states for $J_3 = 0$.

Finally, using that $\cos^2(\phi) + \sin^2(\phi) = 1$, we derive

$$\cos(Q_a) + \cos(Q_b) + \cos(Q_a + Q_b) = \frac{1}{2}\left(\frac{1}{4J_2^2} - 3\right). \tag{C24}$$

The last equation (C24) determines the set of degenerate wavevectors (Q_a, Q_b) in the ground state, while the two equations (C18) and (C23) set the phase difference for a given value of $\boldsymbol{Q}$.

2. Case of nonzero J_3

Let us now discuss the case of nonzero J_3, where the set of equations $\frac{\partial E}{\partial Q_a} = \frac{\partial E}{\partial Q_b} = \frac{\partial E}{\partial \phi} = 0$ reads

$$\begin{aligned}\sin(Q_a + Q_b - \phi) = {} & 2J_2[\sin(Q_a) + \sin(Q_a + Q_b)] \\ & - J_3[2\cos(Q_b - \phi)\sin(Q_a + Q_b) \\ & + \sin(Q_a - \phi)],\end{aligned} \tag{C25}$$

$$\begin{aligned}&\sin(Q_b - \phi) + \sin(Q_a + Q_b - \phi) \\ &\quad = J_2[\sin(Q_b) + \sin(Q_a + Q_b)] - 2J_3\sin(Q_a + 2Q_b - \phi),\end{aligned} \tag{C26}$$

$$\begin{aligned}&\sin(\phi) - \sin(Q_b - \phi) - \sin(Q_a + Q_b - \phi) \\ &\quad = J_3[\sin(Q_a - \phi) + 2\cos(Q_a + Q_b)\sin(Q_b - \phi)].\end{aligned} \tag{C27}$$

We will restrict our attention to sufficiently small J_3, where we numerically find that a set of six symmetry-related wave vectors are selected from the continuous manifold of wave vectors defined by Eq. (C24). Numerically, we find that for $J_3 > 0$ one of them is given by $Q_a = Q_b$, while for $J_3 < 0$ one of them is given by $(Q_a, Q_b) = (Q_a, 0)$. The other five are obtained by C_6 rotations. In Fig. 12 we show numerical results for $J_3 = 0$ and for small values of J_3, which shows that six discrete wavevectors are selected by nonzero J_3, which are of the form described above.

a. Antiferromagnetic $J_3 > 0$

Numerically, we find that the wavevector solution is given by $Q_a = Q_b$ for $J_3 > 0$. In this case, the three equations (C25)–(C27) simplify to

$$\begin{aligned}\sin(2Q_a - \phi) = {} & 2J_2[\sin(Q_a) + \sin(2Q_a)] \\ & - J_3[2\cos(Q_a - \phi)\sin(2Q_a) \\ & + \sin(Q_a - \phi)],\end{aligned} \tag{C28}$$

$$\begin{aligned}&\sin(Q_a - \phi) + \sin(Q_a + Q_a - \phi) \\ &\quad = J_2[\sin(Q_a) + \sin(2Q_a)] - 2J_3\sin(3Q_a - \phi),\end{aligned} \tag{C29}$$

$$\begin{aligned}&\sin(\phi) - \sin(Q_a - \phi) - \sin(2Q_a - \phi) \\ &\quad = J_3[\sin(Q_a - \phi) + 2\cos(2Q_a)\sin(Q_a - \phi)].\end{aligned} \tag{C30}$$

In the third equation (C30), we can use that $\sin(\phi) - \sin(2Q_a - \phi) = -2\cos(Q_a)\sin(Q_a - \phi)$ to bring it into the following form:

$$\sin(Q_a - \phi)[1 + 2\cos(Q_a) + J_3[1 + 2\cos(2Q_a)]] = 0. \tag{C31}$$

This equation can be fulfilled either by $\sin(Q_a - \phi) = 0$ or if the term in the square brackets vanishes, which is the case when $\cos(Q_a) = -1/2$ (K-point) or when $\cos(Q_a) = (-1 + J_3)/(2J_3)$. Note that in the latter case, the wavevector is independent of J_2.

The first case $\sin(Q_a - \phi) = 0$ is the case of interest to us, as we know (e.g., from a numerical investigation) that Q_a depends on J_2 in the region $J_2 > J_3 > 0$, in which we are mostly interested. Therefore, Eq. (C30) gives a condition for ϕ as a function of the wavevector Q_a. In fact, the same condition applies to the case $J_3 = 0$, which means that the solution for ϕ at the minimum is independent of J_3 and identical to our previous solution in Eqs. (C18) and (C23).

Assuming that $\sin(Q_a - \phi) = 0$ in the following, we find that the first and second equations (C28) and (C29) are identical and read

$$\begin{aligned}&2J_2[\sin(Q_a) + \sin(2Q_a)] - 2J_3\cos(Q_a - \phi)\sin(2Q_a) \\ &\quad = \sin(Q_a)\cos(Q_a - \phi).\end{aligned} \tag{C32}$$

Since $\sin(Q_a - \phi) = 0$, it immediately follows that $\cos(Q_a - \phi) = \pm 1$. Solving the above equation in the two cases yields

$$\cos(Q_a) = \frac{1 - 2J_2}{4(J_2 - J_3)} \text{ for } \cos(Q_a - \phi) = 1, \tag{C33}$$

$$\cos(Q_a) = \frac{-1 - 2J_2}{4(J_2 + J_3)} \text{ for } \cos(Q_a - \phi) = -1. \tag{C34}$$

It turns out that the first solution is the relevant one in the regime $J_2 > 0$. We thus find that

$$Q_a = 2\pi H = \arccos\frac{1 - 2J_2}{4(J_2 - J_3)}. \tag{C35}$$

Finally, the experimentally observed wavevector $H = K = 1/6$ is found for

$$J_2(J_1, J_3) = \tfrac{1}{4}(J_1 + 2J_3). \tag{C36}$$

Therefore, to observe $H = K = 1/6$, we need an antiferromagnetic $J_3 > 0$, and the required second-neighbor exchange

J_2 increases with the value of J_3. Note that this corresponds to a highly frustrated set of coupling constants. In the next section, we show that a finite sixfold single-ion anisotropy significantly increases the phase space of the $H = K = 1/6$ solution in the model.

3. Effect of finite sixfold single-ion anisotropy D_{xy}

Let us now determine the effect of a sixfold in-plane single-ion anisotropy term that is allowed by symmetry:

$$H_{D_{xy}} = \frac{D_{xy}}{2} \sum_{R_i} \sum_{\alpha=A,B} \left\{ \left[S^x_\alpha(R_i) + iS^y_\alpha(R_i) \right]^6 + \left[S^x_\alpha(R_i) - iS^y_\alpha(R_i) \right]^6 \right\}. \tag{C37}$$

Inserting the spin ansatz in Eq. (C9) and focusing on the solutions with $H = K$ that we found for $J_3 > 0$, we find that [see also Fig. 7(b)]

$$\frac{E_{D_{xy}}}{NS^6} = -D_{xy}(\delta_{H,1/6} + \delta_{H,1/3}). \tag{C38}$$

Note that to determine $E_{D_{xy}}$ for states with $H \neq K$, we would first need to solve for the phase ϕ of those states analytically. Instead, we have investigated the problem numerically for general (H, K) and ϕ [see Fig. 7(b)]. From Eq. (C38) we observe that states with $H = K = 1/3$ and $H = K = 1/6$ are favored by D_{xy} because they are compatible with the sixfold anisotropy on every site. Spiral states with any other wave vector yield an average energy of zero in the limit of large system sizes as every angle occurs at some site, and the average anisotropy thus vanishes. To determine the region in the phase diagram where spirals with $H = 1/6$ are stabilized as a function of D_{xy}, we compare the energy of the spiral found for $D_{xy} = 0$ with the energy of the spiral with $H = 1/6$ and finite D_{xy}, and the results are given in Figs. 7(c) and 7(d).

[1] J. Chaloupka, G. Jackeli, and G. Khaliullin, Kitaev-Heisenberg Model on a Honeycomb Lattice: Possible Exotic Phases in Iridium Oxides A_2IrO_3, Phys. Rev. Lett. **105**, 027204 (2010).

[2] S. Trebst and C. Hickey, Kitaev materials, Phys. Rep. **950**, 1 (2022).

[3] J. R. Morey, A. Scheie, J. P. Sheckelton, C. M. Brown, and T. M. McQueen, $Ni_2Mo_3O_8$: Complex antiferromagnetic order on a honeycomb lattice, Phys. Rev. Mater. **3**, 014410 (2019).

[4] M. Yehia, E. Vavilova, A. Möller, T. Taetz, U. Löw, R. Klingeler, V. Kataev, and B. Büchner, Finite-size effects and magnetic order in the spin-1/2 honeycomb-lattice compound $InCu_{2/3}V_{1/3}O_3$, Phys. Rev. B **81**, 060414(R) (2010).

[5] M. Iakovleva, O. Janson, H.-J. Grafe, A. P. Dioguardi, H. Maeter, N. Yeche, H.-H. Klauss, G. Pascua, H. Luetkens, A. Möller, B. Büchner, V. Kataev, and E. Vavilova, Ground state and low-temperature magnetism of the quasi-two-dimensional honeycomb compound $InCu_{2/3}V_{1/3}O_3$, Phys. Rev. B **100**, 144442 (2019).

[6] O. Smirnova, M. Azuma, N. Kumada, Y. Kusano, M. Matsuda, Y. Shimakawa, T. Takei, Y. Yonesaki, and N. Kinomura, Synthesis, crystal structure, and magnetic properties of $Bi_3Mn_4O_{12}(NO_3)$ Oxynitrate Comprising $S = 3/2$ Honeycomb Lattice, J. Am. Chem. Soc. **131**, 8313 (2009).

[7] S. Miyamoto, Y. Iwasaki, N. Uemoto, Y. Hosokoshi, H. Fujiwara, S. Shimono, and H. Yamaguchi, Magnetic properties of honeycomb-based spin models in verdazyl-based salts, Phys. Rev. Mater. **3**, 064410 (2019).

[8] A. Kitaev, Anyons in an exactly solved model and beyond, Ann. Phys. **321**, 2 (2006).

[9] G. Baskaran, D. Sen, and R. Shankar, Spin-S Kitaev model: Classical ground states, order from disorder, and exact correlation functions, Phys. Rev. B **78**, 115116 (2008).

[10] J. Reuther, R. Thomale, and S. Trebst, Finite-temperature phase diagram of the Heisenberg-Kitaev model, Phys. Rev. B **84**, 100406(R) (2011).

[11] C. Price and N. B. Perkins, Finite-temperature phase diagram of the classical Kitaev-Heisenberg model, Phys. Rev. B **88**, 024410 (2013).

[12] E. Rastelli, A. Tassi, and L. Reatto, Non-simple magnetic order for simple Hamiltonians, Physica B+C **97**, 1 (1979).

[13] S. Katsura, T. Ide, and T. Morita, The ground states of the classical heisenberg and planar models on the triangular and plane hexagonal lattices, J. Stat. Phys. **42**, 381 (1986).

[14] J. Fouet, P. Sindzingre, and C. Lhuillier, An investigation of the quantum J_1-J_2-J_3 model on the honeycomb lattice, Eur. Phys. J. B **20**, 241 (2001).

[15] A. Mulder, R. Ganesh, L. Capriotti, and A. Paramekanti, Spiral order by disorder and lattice nematic order in a frustrated Heisenberg antiferromagnet on the honeycomb lattice, Phys. Rev. B **81**, 214419 (2010).

[16] A. F. Albuquerque, D. Schwandt, B. Hetényi, S. Capponi, M. Mambrini, and A. M. Läuchli, Phase diagram of a frustrated quantum antiferromagnet on the honeycomb lattice: Magnetic order versus valence-bond crystal formation, Phys. Rev. B **84**, 024406 (2011).

[17] J. Reuther, D. A. Abanin, and R. Thomale, Magnetic order and paramagnetic phases in the quantum J_1-J_2-J_3 honeycomb model, Phys. Rev. B **84**, 014417 (2011).

[18] J. Oitmaa and R. R. P. Singh, Phase diagram of the J_1-J_2-J_3 Heisenberg model on the honeycomb lattice: A series expansion study, Phys. Rev. B **84**, 094424 (2011).

[19] B. K. Clark, D. A. Abanin, and S. L. Sondhi, Nature of the Spin Liquid State of the Hubbard Model on a Honeycomb Lattice, Phys. Rev. Lett. **107**, 087204 (2011).

[20] R. F. Bishop, P. H. Y. Li, D. J. J. Farnell, and C. E. Campbell, The frustrated Heisenberg antiferromagnet on the honeycomb lattice: J_1-J_2 model, J. Phys.: Condens. Matter **24**, 236002 (2012).

[21] R. F. Bishop, P. H. Y. Li, and C. E. Campbell, Valence-bond crystalline order in the $s = 1/2 J_1$-J_2 model on the honeycomb lattice, J. Phys.: Condens. Matter **25**, 306002 (2013).

[22] R. F. Bishop, P. H. Y. Li, O. Götze, J. Richter, and C. E. Campbell, Frustrated Heisenberg antiferromagnet on the honeycomb lattice: Spin gap and low-energy parameters, Phys. Rev. B **92**, 224434 (2015).

[23] J. Sahoo and R. Flint, Symmetric spin liquids on the stuffed honeycomb lattice, Phys. Rev. B **101**, 115103 (2020).

[24] X.-Y. Dong and D. N. Sheng, Spin-1 Kitaev-Heisenberg model on a honeycomb lattice, Phys. Rev. B **102**, 121102(R) (2020).

[25] H.-K. Jin, W. M. H. Natori, F. Pollmann, and J. Knolle, Unveiling the S=3/2 Kitaev honeycomb spin liquids, Nat. Commun. **13**, 3813 (2022).

[26] N. S. Sangeetha, S. Pakhira, Q.-P. Ding, L. Krause, H.-C. Lee, V. Smetana, A.-V. Mudring, B. B. Iversen, Y. Furukawa, and D. C. Johnston, First-order antiferromagnetic transitions of $SrMn_2P_2$ and $CaMn_2P_2$ single crystals containing corrugated-honeycomb Mn sublattices, Proc. Natl. Acad. Sci. USA **118**, e2108724118 (2021).

[27] N. S. Sangeetha, A. Pandey, Z. A. Benson, and D. C. Johnston, Strong magnetic correlations to 900 K in single crystals of the trigonal antiferromagnetic insulators $SrMn_2As_2$ and $CaMn_2As_2$, Phys. Rev. B **94**, 094417 (2016).

[28] J. W. Simonson, G. J. Smith, K. Post, M. Pezzoli, J. J. Kistner-Morris, D. E. McNally, J. E. Hassinger, C. S. Nelson, G. Kotliar, D. N. Basov, and M. C. Aronson, Magnetic and structural phase diagram of $CaMn_2Sb_2$, Phys. Rev. B **86**, 184430 (2012).

[29] N. S. Sangeetha, V. Smetana, A.-V. Mudring, and D. C. Johnston, Antiferromagnetism in semiconducting $SrMn_2Sb_2$ and $BaMn_2Sb_2$ single crystals, Phys. Rev. B **97**, 014402 (2018).

[30] P. Das, N. S. Sangeetha, A. Pandey, Z. A. Benson, T. W. Heitmann, D. C. Johnston, A. I. Goldman, and A. Kreyssig, Collinear antiferromagnetism in trigonal $SrMn_2As_2$ revealed by single-crystal neutron diffraction, J. Phys.: Condens. Matter **29**, 035802 (2017).

[31] C. Bridges, V. Krishnamurthy, S. Poulton, M. Paranthaman, B. Sales, C. Myers, and S. Bobev, Magnetic order in $CaMn_2Sb_2$ studied via powder neutron diffraction, J. Magn. Magn. Mater. **321**, 3653 (2009).

[32] Q. D. Gibson, H. Wu, T. Liang, M. N. Ali, N. P. Ong, Q. Huang, and R. J. Cava, Magnetic and electronic properties of $CaMn_2Bi_2$: A possible hybridization gap semiconductor, Phys. Rev. B **91**, 085128 (2015).

[33] W. Ratcliff II, A. Lima Sharma, A. Gomes, J. Gonzalez, Q. Huang, and J. Singleton, The magnetic ground state of $CaMn_2Sb_2$, J. Magn. Magn. Mater. **321**, 2612 (2009).

[34] F. Islam, E. Gordon, P. Das, Y. Liu, L. Ke, D. L. Abernathy, R. J. McQueeney, and D. Vaknin, Spin dynamics in antiferromagnetic oxypnictides and fluoropnictides: LaMnAsO, LaMnSbO, and BaMnAsF, Phys. Rev. B **101**, 155119 (2020).

[35] S. L. Brock, J. Greedan, and S. M. Kauzlarich, Resistivity and magnetism of AMn_2P_2 (A = Sr, Ba): The effect of structure type on physical properties, J. Solid State Chem. **113**, 303 (1994).

[36] A. Little, C. Lee, C. John, S. Doyle, E. Maniv, N. L. Nair, W. Chen, D. Rees, J. W. F. Venderbos, R. M. Fernandes, J. G. Analytis, and J. Orenstein, Three-state nematicity in the triangular lattice antiferromagnet $Fe_{1/3}NbS_2$, Nat. Mater. **19**, 1062 (2020).

[37] R. M. Fernandes, P. P. Orth, and J. Schmalian, Intertwined vestigial order in quantum materials: Nematicity and beyond, Annu. Rev. Condens. Matter Phys. **10**, 133 (2019).

[38] D. E. McNally, J. W. Simonson, J. J. Kistner-Morris, G. J. Smith, J. E. Hassinger, L. DeBeer-Schmitt, A. I. Kolesnikov, I. A. Zaliznyak, and M. C. Aronson, $CaMn_2Sb_2$: Spin waves on a frustrated antiferromagnetic honeycomb lattice, Phys. Rev. B **91**, 180407(R) (2015).

[39] J. Perez-Mato, S. Gallego, E. Tasci, L. Elcoro, G. de la Flor, and M. Aroyo, Symmetry-based computational tools for magnetic crystallography, Annu. Rev. Mater. Res. **45**, 217 (2015).

[40] N. Ni, S. Nandi, A. Kreyssig, A. I. Goldman, E. D. Mun, S. L. Bud'ko, and P. C. Canfield, First-order structural phase transition in $CaFe_2As_2$, Phys. Rev. B **78**, 014523 (2008).

[41] R. M. Fernandes, A. V. Chubukov, J. Knolle, I. Eremin, and J. Schmalian, Preemptive nematic order, pseudogap, and orbital order in the iron pnictides, Phys. Rev. B **85**, 024534 (2012).

[42] W. Janke and R. Villanova, Three-dimensional 3-state Potts model revisited with new techniques, Nucl. Phys. B **489**, 679 (1997).

[43] Y. J. Li, F. Jin, Z. Y. Mi, J. Guo, W. Wu, Z. H. Yu, D. S. Wu, S. H. Na, C. Mu, X. B. Zhou, Z. Li, K. Liu, L. L. Sun, Q. M. Zhang, T. Xiang, G. Li, and J. L. Luo, First-order transition in trigonal structure $CaMn_2P_2$, Europhys. Lett. **132**, 46001 (2020).